Single-Photon Interference in Young's Double-Slit Experiment: Fraunhofer and Path-Integral Models of Diffraction

Chidiebube Enwereji
Department of Physics and Astronomy, Dartmouth College, Hanover, NH 03755
(Dated: June 19, 2026)

We present a quantitative study of Young's double-slit interference performed in both classical and single-photon regimes. Filtered light from an incoherent thermal bulb is attenuated to a count rate of ~ 300 photons per second, with the photon time-of-flight through the apparatus (~ 3 ns) more than four orders of magnitude shorter than the mean inter-arrival time (~ 130 µs), so that the probability of two photons being simultaneously in flight is of order 10^{-9}. We verify the Poisson character of the photon counting process directly from repeated 1-second samples at 28 detector positions and fit the resulting single-slit and double-slit interference patterns to two diffraction models: the standard far-field Fraunhofer expression, and a Fresnel sum-over-paths model that retains the quadratic-in-displacement phase terms appropriate to our finite-distance geometry. Both models reproduce the single-slit envelopes equally well, but on the double-slit data the path-integral model outperforms Fraunhofer by a factor of seven in χ^2/ν and recovers a slit width consistent with the single-slit fits — a difference quantitatively predicted by the dimensionless Fresnel parameter $F = L_\perp/\sqrt{\lambda D}$, which for our double-slit geometry is ≈ 0.77. Cross-checks against laser-illuminated data confirm the same picture.

I. INTRODUCTION

Thomas Young's 1807 double-slit experiment was the first compelling demonstration of the wave nature of light, and it remains a centerpiece of physics pedagogy today [1]. By the close of the nineteenth century, dynamical theories of light due to Fresnel and Maxwell seemed to have made the wave picture canon. However, the twentieth century introduced some complications: Planck's hypothesis, Einstein's explanation of the photoelectric effect [2], and Compton's scattering measurements established that light is exchanged in discrete quanta, ushering in the concept of the photon and inviting the natural question of what becomes of Young's interference fringes when the light is so dim that only one photon at a time is in the apparatus.

This question is no longer hypothetical. Beginning with G. I. Taylor's classic 1909 experiment using a smoke-attenuated candle [3], a sequence of increasingly refined measurements has confirmed that interference fringes accumulate one photon click at a time, with no qualitative difference from the patterns produced by a coherent classical wave. Modern implementations have replaced thermal sources with spontaneous parametric down-conversion to produce heralded single photons [4, 5], but a thermal source at sufficiently low intensity remains operationally adequate: the probability of multi-photon occupancy can be driven arbitrarily small by dimming the source. What such experiments dramatize is not so much the existence of photons or of wave behavior in isolation, but rather their coexistence in a single apparatus, which forces a quantum-mechanical reinterpretation of "interference" as the coherent addition of probability amplitudes for indistinguishable paths rather than the spatial superposition of two physical waves [6].

In this paper we report a quantitative study of single-photon interference using a two-slit apparatus that allows the same Young's experiment to be performed sequentially with a coherent laser source and an attenuated thermal bulb without disturbing the optical alignment. We record three diffraction scans in the single-photon regime — two single-slit reference envelopes (with one slit physically blocked) and one double-slit fringe pattern — and verify that the underlying photon arrival process is Poisson, with a count-rate scaling $\sigma_{n-1} = \sqrt{\bar{N}}$ confirmed empirically across more than an order of magnitude in mean count rate. We then fit the patterns to two models of diffraction. The first is the textbook Fraunhofer expression [7], which assumes infinitely distant source and detector. The second is a path-integral model based on Feynman's sum-over-paths prescription [6, 8], evaluated in the Fresnel approximation appropriate to our finite-distance geometry, with incoherent integration over the source-slit and detector-slit widths. The two models reduce to one another in the Fraunhofer limit; the question we address is whether the additional machinery of the path-integral treatment is justified by the data, and where in the geometry the distinction matters.

II. THEORY AND METHOD

A. Young's Double Slit

The wave theory of light is supported by the behavior of light passing through narrow apertures: the light bends around the gaps, as is characteristic of wave-like disturbances. Young's double-slit experiment is the canonical demonstration of this phenomenon. A coherent light wave is produced by passing light from some source through a single slit; this light then passes through two closely spaced slits, producing an interference pattern on a screen some distance downstream.

The pattern consists of alternating bright and dark fringes, and it is explained by the phase difference introduced by the path-length difference between light from each slit reaching the same point on the screen, as shown in Fig. 1. This geometric picture accounts for the *locations* of the fringes but says little about their *intensities*; for that, a more quantitative model is needed.

The simplest such model assumes Fraunhofer diffraction, in which the light source and detector are treated as infinitely far from the slits so that incoming and outgoing wavefronts are planar. Under these assumptions, the intensity as a function of the angular variable θ, measured in radians from the central axis of the apparatus, is [7]

$$I(\theta) = I_0 \cos^2(\beta) \left(\frac{\sin\alpha}{\alpha} \right)^2 , \tag{1}$$

where

$$\alpha = \frac{\pi a \sin\theta}{\lambda}, \qquad \beta = \frac{\pi d \sin\theta}{\lambda}, \tag{2}$$

a is the slit width, d is the center-to-center slit separation, λ is the wavelength of the light, and I_0 is the intensity at the central maximum. The two factors in Eq. (1) have distinct physical origins: the $\cos^2\beta$ term is the two-source interference factor arising from the phase difference between light from the two slits, while the $(\sin\alpha/\alpha)^2$ envelope is the single-slit diffraction pattern arising from the finite width of each slit. We discuss this model and other models of diffraction further in Section V.

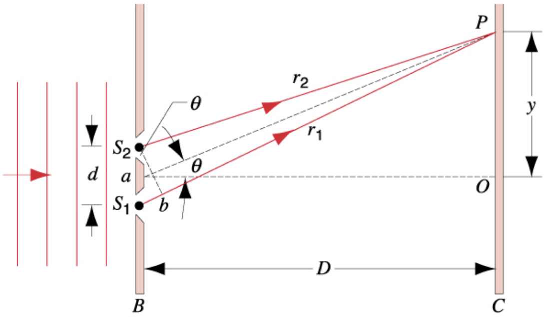

FIG. 1. Geometry of Young's double-slit experiment. Light from a distant source passes through two narrow slits separated by d and produces a pattern of bright and dark fringes on a screen a distance L downstream. The fringe locations are determined by the path-length difference between the two paths.

B. Single Photon Regime

Light is no longer regarded as purely wavelike. From Planck's hypothesis through the photoelectric and Compton effects, the particle nature of light has been firmly established, and this introduces an apparent paradox: the geometric interpretation of interference described above seems untenable when only a few photons pass through the slits at a time, and impossible when only one does. The resolution is that the quantized character of light demands a quantum-mechanical interpretation of the experiment. The fringes no longer represent a continuous intensity distribution but rather the probability of detecting a photon at a given location on the screen, and "interference" takes on an altogether different meaning: rather than two physical waves superposing in space, it is the probability amplitudes associated with the two possible paths through the slits that add coherently, with the observed photon distribution given by the squared magnitude of their sum,

$$P(x) = |\psi_1(x) + \psi_2(x)|^2 , \tag{3}$$

where ψ_1 and ψ_2 are the complex amplitudes for the photon to reach position x via slit 1 or slit 2, respectively [6]. The goal of this experiment is to show that the same fringe pattern emerges in the single-photon regime as from a coherent classical wave, even though only one photon at a time is sent through the slits.

III. APPARATUS AND SYSTEMATICS

A. Apparatus

As shown in Fig. 2, the apparatus consists of a long rectangular assembly housing two light sources at its left end: a red diode laser ($\lambda = 670 \pm 5$ nm, output power ~ 5 mW) and a green-filtered incandescent bulb (passing wavelengths in the range 541–551 nm). Light from the selected source passes through a source slit of width 0.085 mm, then propagates 38 cm downstream to the double-slit assembly, whose slits are each 0.085 mm wide with a nominal center-to-center separation of $d \approx 0.4$ mm. Immediately downstream of the double slit is a slit-blocker, a wide aperture mounted on a micrometer-driven flexure stage that can be translated laterally to block light from either slit, both slits, or neither. The light then propagates approximately 50 cm to the detector slit, also 0.085 mm wide and likewise micrometer-positioned, which selects a narrow vertical slice of the interference pattern to deliver to the detector module at the right end of the apparatus.

The apparatus is used in two modes. In the classical mode, the red laser illuminates the slit system and the transmitted light is recorded by a solid-state photodiode operated as a current source; the photocurrent is converted to a voltage by an on-board transimpedance amplifier (22×10^6 V/A) and read on a digital multimeter. The photodiode signal is proportional to the incident optical power and is used to reproduce the classically predicted interference fringes. In the single-photon mode, the laser is moved aside and the filtered bulb is used

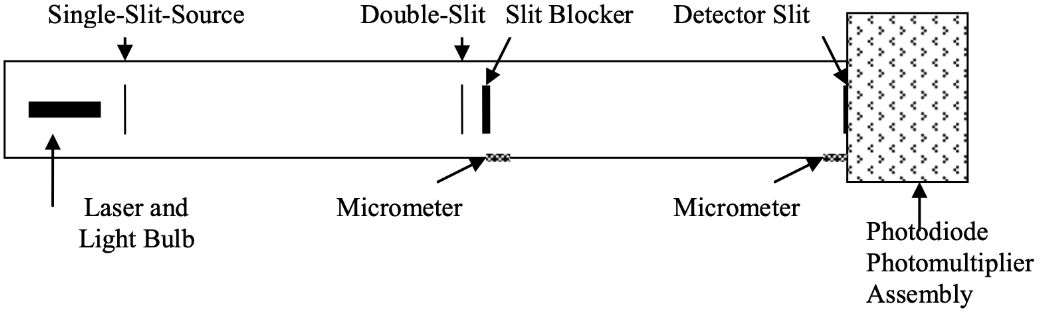

FIG. 2. Schematic of the two-slit apparatus. Light from either the red diode laser or the green-filtered incandescent bulb passes through a source slit, propagates 38 cm to the double-slit assembly, then a further 50 cm to a movable detector slit. In classical mode, the laser is selected and the transmitted intensity is recorded by a photodiode; in single-photon mode, the bulb is selected and individual photons are counted by a photomultiplier tube.

instead. The bulb produces a broadband thermal spectrum; the green filter passes only a 10 nm band, and the bulb's intensity is further reduced to such a low level that, by the argument given in Section III B, photons traverse the apparatus essentially one at a time. The transmitted photons are detected by a photomultiplier tube (PMT) housed in the detector module behind a protective shutter, with the photodiode mechanically swung out of the optical path.

The PMT and its associated photo-electronics comprise two principal stages: the PMT itself, followed by a pulse amplifier and discriminator. At the PMT photocathode, incident photons liberate photoelectrons via the photoelectric effect with a quantum efficiency of approximately 4% for green light; these photoelectrons are accelerated through a chain of dynodes biased by a high-voltage supply (0–1000 V), with each dynode multiplying the electron bunch through secondary emission to a final gain of order 10^5–10^6. The resulting charge pulse is converted to a voltage pulse by a charge-sensitive amplifier and compared against an adjustable discriminator threshold; pulses exceeding the threshold trigger a fixed-width TTL output, which is sent to a counter set to record events in 1-second intervals. Two adjustable parameters therefore govern the recorded signal: the dynode high voltage, which sets the PMT gain, and the discriminator threshold, which sets the minimum detectable pulse amplitude.

B. Single Photon Regime Justification

To verify that the apparatus operates in a regime where photons traverse the slits essentially one at a time, we compare two timescales: the mean time between successive photon arrivals at the PMT photocathode, and the time of flight of a photon through the apparatus. Under typical operating conditions with the bulb dimmed and the green filter in place, we recorded a central-maximum count rate of approximately 300 events per second. Given the PMT's ∼4% quantum efficiency for green light, the true rate of photons arriving at the photocathode is

$$R = \frac{300\ \mathrm{s}^{-1}}{0.04} \approx 7.5 \times 10^3\ \text{photons/s}, \qquad (4)$$

corresponding to a mean inter-arrival time of $\tau_{\text{between}} = 1/R \approx 130\ \mu\text{s}$. The total optical path length from bulb to detector is approximately $L \approx 1$ m, giving a photon time of flight

$$t_{\text{flight}} = \frac{L}{c} \approx 3.3\ \text{ns}. \qquad (5)$$

The fraction of time during which at least one photon is in flight through the apparatus is therefore $f = t_{\text{flight}}/\tau_{\text{between}} \approx 2.5 \times 10^{-5}$. Because photon arrivals from a thermal source at low intensity obey Poisson statistics — which we verify directly in Section IV A — the probability of two photons being in flight simultaneously is the square of this fraction, $f^2 \approx 6 \times 10^{-10}$. Essentially every detected photon traverses the apparatus alone.

C. PMT Systematics

The photon signal incident on the PMT photocathode is converted to a photoelectron current and amplified through a chain of dynodes held at progressively higher voltages. Each stage takes a finite time to accelerate and multiply the electron bunch, so the end-to-end electron transit time through the PMT is on the order of tens of nanoseconds. This fixed delay displaces every recorded event from the true moment of photon arrival by a roughly constant offset; since our measurements are of *count rates* rather than absolute arrival times, this offset has no effect on the data and is absorbed implicitly.

A more directly relevant PMT effect is gain instability with bias voltage. The gain of the dynode chain rises exponentially with the applied high voltage, reaching $\sim 10^6$ near full bias, so small drifts in the high-voltage setting translate into substantial drifts in detected count rate at fixed light level. We chose an operating voltage in the plateau region of the dark-rate-versus-bias curve (around 5 turns of the 10-turn dial), where the count rate is no longer rising steeply with voltage and is thus relatively insensitive to small drifts. All scans were taken at a single fixed bias voltage to ensure consistent gain across the dataset.

D. Signal Ringing and PMT Pileup

The dynode chain is a capacitive structure, and the trailing edge of a PMT pulse can undershoot the baseline and oscillate before settling. If the ringing amplitude crosses the discriminator threshold, a single physical photon event fires the electronics multiple times, producing spurious extra counts at characteristic sub-microsecond intervals after every genuine event. We calibrated the discriminator threshold by viewing the analog and TTL pulse trains simultaneously on a dual-trace oscilloscope and selecting a threshold low enough to register essentially every real analog pulse but high enough that no TTL pulses appeared without a corresponding analog event.

A related concern is pulse pileup: if two photon events arrive within the $\sim$ 100 ns dead time of the amplifier-discriminator chain, they are recorded as a single event. At our central-maximum count rate of 300 s^{-1}, the mean inter-arrival time of 130 µs is more than three orders of magnitude longer than the dead time, so pileup losses are negligible ($\sim 10^{-5}$).

E. Dark Rate and Background Subtraction

Even with the PMT shutter closed and no light entering the apparatus, the PMT registers a finite “dark rate” arising from thermal emission of electrons at the photocathode and from spurious pulses in the amplifier chain. An additional background contribution arises when the bulb is on but both slits are blocked by the slit-blocker, accounting for any stray light reaching the detector that has not passed through the two-slit assembly. To isolate the signal due to genuine photon events arriving through the slits, we measured this background rate periodically throughout each scan — with both slits blocked under the same bulb and PMT settings used for data collection — and subtracted the resulting count rate from every measurement. This background-corrected count rate is what we report and compare to theory throughout the remainder of this paper.

IV. DATA AND ANALYSIS

A. Photon Arrival Statistics

Before fitting the diffraction patterns we verify that the photon counting process is governed by Poisson statistics, so that the appropriate per-point uncertainty for a counted signal n is $\sigma = \sqrt{n}$. Photon emission from a thermal source at very low intensity is, classically, a Poisson process: independent emission events at a constant mean rate, with the random pruning of the detection step preserving the Poisson character of the recorded counts. The Poisson distribution has variance equal to its mean,

$$\mathrm{Var}(n) = \bar{n}, \qquad \sigma_n = \sqrt{\bar{n}}. \tag{6}$$

We tested this prediction empirically with a dedicated scan in which each detector-slit position was sampled $n = 8$ times with 1-second integrations, holding all other settings fixed. The detector slit was stepped across the same range as the diffraction scans, so that positions near the central maximum recorded $\bar{N} \sim 90$ counts/s while positions in the wings recorded $\bar{N} \sim 8$ counts/s — spanning more than an order of magnitude in mean count rate at a single bulb intensity. At each of 28 positions we computed the sample mean $\bar{N}$ and the sample standard deviation σ_{n-1} (with Bessel’s correction) across the 8 replicates, and tested the Poisson prediction $\sigma_{n-1} = \sqrt{\bar{N}}$.

The results are shown in Fig. 3. The mean of the ratio $\sigma_{n-1}/\sqrt{\bar{N}}$ across the 28 positions is 0.91 with sample standard deviation 0.28, fully consistent with the Poisson value of unity given the scatter expected from finite-sample statistics. For n samples of a Poisson variable, the sample standard deviation σ_{n-1} itself fluctuates with relative uncertainty $1/\sqrt{2(n-1)}$ [9], which for $n = 8$ gives a theoretical scatter of 0.27 — matching the observed scatter of 0.28 almost exactly. No systematic deviation from $\sigma \propto \sqrt{\bar{N}}$ is visible across the full count range.

Having verified the Poisson character of the counting process, we note that all data points in the diffraction scans presented below fall in the count range $80 \lesssim N \lesssim 3400$ per 10-second integration. In this regime the Poisson distribution is very well approximated by a Gaussian of equal mean and variance: the relative skewness $1/\sqrt{\bar{N}}$ is at most 0.11 even for the lowest-count bins, so the Gaussian approximation to the Poisson is essentially exact across the entire dataset. We may therefore use the standard χ^2 statistic with Poisson weights $\sigma_i = \sqrt{n_i}$ in the fits that follow, without resorting to a full Poisson likelihood treatment.

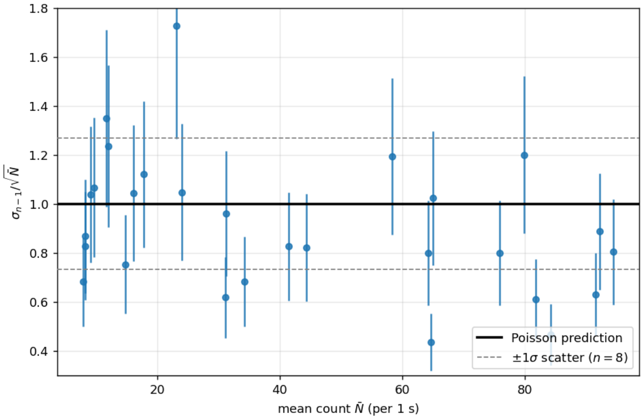

FIG. 3. Verification of Poisson photon statistics. At each of 28 detector-slit positions, $n = 8$ independent 1-second photon counts were recorded; the ratio of the sample standard deviation σ_{n-1} to the Poisson prediction $\sqrt{\bar{N}}$ is plotted against the sample mean $\bar{N}$. The solid black line marks the Poisson prediction; the dashed lines mark the $\pm1\sigma$ scatter band $\pm1/\sqrt{2(n-1)}$ expected from finite-sample uncertainty on σ_{n-1} [9]. Error bars on each point reflect the same finite-sample uncertainty. The observed mean ratio is 0.91 ± 0.28, consistent with the Poisson value of unity, and shows no systematic trend with mean count.

B. Diffraction Runs

We collected three quantitative scans in the single-photon mode of the apparatus: two single-slit reference patterns with the slit-blocker covering one of the two slits in turn (denoted `single_slit_x2` and `single_slit_x4`), and one full double-slit scan with both slits open. The scans were taken under nominally identical PMT, bulb, and discriminator settings, with the detector-slit micrometer advanced in fixed increments and the photon count accumulated over 10 s at each position. A summary of the three scans is given in Table I.

Scan	Points	Step (mm)	Range (mm)	Peak (cts/10s)	Background (cts/10s)
`single_slit_x2`	25	0.25	0.75–6.75	1128	89
`single_slit_x4`	29	0.25	1.25–8.25	1008	60
`double_slit`	141	0.05	0.75–7.75	3431	67

TABLE I. Summary of the three quantitative scans. The two single-slit runs sample at coarse resolution across the slit-diffraction envelope, while the double-slit run samples five times more densely to resolve the interference fringes.

C. Curve Fitting

We fit the three scans to two models of increasing sophistication: the far-field Fraunhofer model of Section II and the finite-distance sum-over-paths (Fresnel) model derived in Section V A. The wavelength $\lambda = 546$ nm is taken as the midpoint of the green filter passband and held fixed, as are the geometric distances D_1 and D_2 and the source- and detector-slit widths $a_{\rm src} = a_{\rm det} = 0.085$ mm. The measured background B from each scan is held fixed at the value listed in Table I.

For each single-slit scan we fit three parameters: the central-fringe amplitude N_0, the detector position of the central axis x_0, and the slit width a. For the double-slit scan we fit a fourth parameter, the center-to-center slit separation d:

$$N(x) = N_0\,\mathcal{I}(x; x_0, a, d) + B, \tag{7}$$

where $\mathcal{I}(x;\cdot)$ is the predicted intensity under the chosen model. The two models differ only in how $\mathcal{I}$ is computed; the parameter list is identical.

The slit width a and separation d are treated as free fit parameters rather than fixed to their nominal values, allowing the data to constrain the apparatus geometry directly. This choice inverts the conventional textbook framing in which the slit dimensions are taken as known inputs and the predicted fringe pattern is compared to data; here we instead ask what slit dimensions are consistent with the observed pattern under each model. Consistency of the fitted a across the three independent scans (Table II) provides an internal cross-check that the fit is recovering a real physical parameter rather than absorbing model mis-specification: any reasonable model should return the same slit width whether one or both slits are open. We did this because we could not definitively characterize the slit separation with any available measurement apparatus and there were three distinct possibilities for its value.

Photon counting at each detector position is a Poisson process, so we weight each datum by its Poisson uncertainty $\sigma_i = \sqrt{n_i}$ and minimize the standard χ^2 statistic,

$$\chi^2 = \sum_i \frac{[n_i - f_i(x_i;\theta)]^2}{n_i}, \tag{8}$$

where f_i is the model prediction at position x_i. Best-fit parameters and their one-sigma uncertainties are extracted from the covariance matrix returned by the fit; results appear in Table II.

Scan	Model	a (μm)	d (μm)	χ^2/ν
`single_slit_x2`	Fraunhofer	84.18 ± 0.67	—	0.47
	Path-integral	84.25 ± 0.67	—	0.47
`single_slit_x4`	Fraunhofer	82.24 ± 0.64	—	2.67
	Path-integral	82.32 ± 0.64	—	2.64
`double_slit`	Fraunhofer	79.41 ± 0.18	398.94 ± 0.17	31.18
	Path-integral	83.15 ± 0.21	399.96 ± 0.21	4.30

TABLE II. Best-fit slit width a, slit separation d, and reduced chi-squared χ^2/ν for each scan under each model. Nominal values are $a = 85$ μm and $d \in \{353, 406, 457\}$ μm depending on which double-slit assembly is installed.

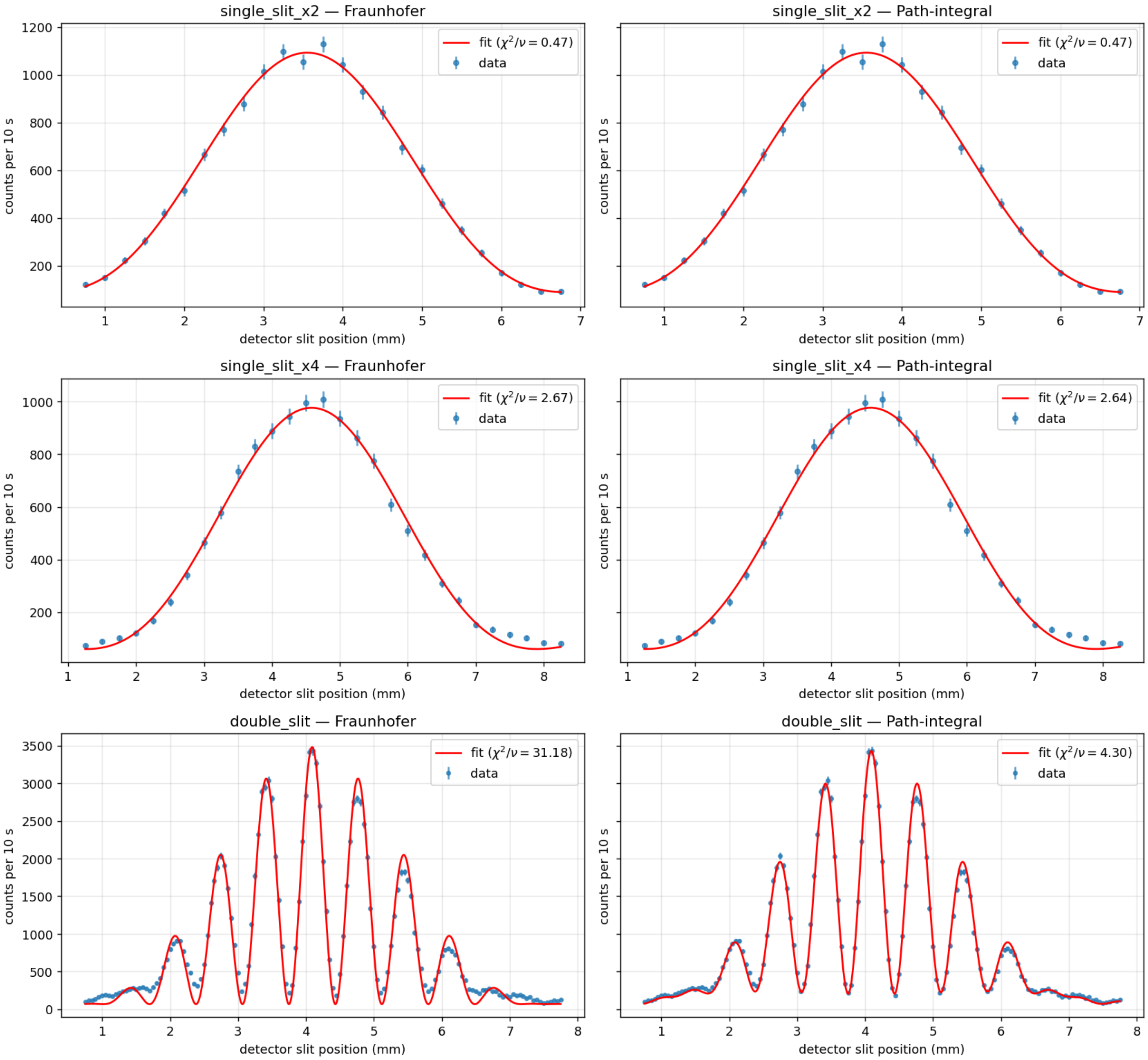

FIG. 4. Fits to the three diffraction scans under two theoretical models. Rows correspond to the three scans (`single_slit_x2`, `single_slit_x4`, `double_slit`); the left column shows fits using the Fraunhofer far-field model, while the right column shows fits using the sum-over-paths Fresnel model derived in Section V A, evaluated analytically via Fresnel C and S integrals and integrated incoherently over the source- and detector-slit widths. Data points show the background-subtracted photon counts per 10 s with Poisson error bars $\sqrt{n}$; the red curve is the best-fit model. Per-panel reduced chi-squared values are reported in each legend. The two models give statistically indistinguishable single-slit fits but differ dramatically on the double-slit data, where the Fraunhofer model systematically over-predicts every fringe peak.

The detector-slit micrometer reading x relates to the model coordinate through a single free offset x_0 (the micrometer value corresponding to the optical axis), fit alongside the other parameters. For the Fraunhofer model this offset enters via the angular variable

$$\sin\theta = \frac{x - x_0}{\sqrt{D_2^2 + (x - x_0)^2}}, \tag{9}$$

while for the path-integral model it enters directly as the transverse detector coordinate $z = x - x_0$.

V. DISCUSSION

A. The Fresnel Sum-Over-Paths Model

The Fraunhofer model used to fit the diffraction patterns above assumes that both the source and detector are infinitely far from the slit plane. Our apparatus violates both assumptions: the source slit sits $D_1 \approx 380$ mm upstream of the double slit, and the detector slit sits $D_2 \approx 500$ mm downstream. A more general treatment is obtained by following Feynman's sum-over-paths prescription [6, 8], in which the amplitude at the detector is built up by adding complex phase factors $\exp(2\pi i s/\lambda)$ along every allowable path from source to detector. Because the opaque double-slit screen blocks every path except those passing through an open aperture, and because free-space propagation between source and slit (and slit and detector) is dominated by straight-line paths, every contributing path is fully specified by a single number: the point y at which it crosses the slit plane.

The path length for a path that goes from source point x to slit-plane point y to detector point z is

$$s(x, y, z) = \sqrt{D_1^2 + (x-y)^2} + \sqrt{D_2^2 + (y-z)^2}, \quad (10)$$

and the complex amplitude at the detector, given a point source at x, is the integral over y of $\exp(2\pi i s/\lambda)$ over the open slit aperture S. Expanding the square roots to lowest non-trivial order in the transverse displacements — the Fresnel approximation, which is justified for our geometry since the off-axis distances are at most a few millimeters compared to $D_1, D_2 \sim$ hundreds of millimeters — the amplitude reduces to

$$U(x, z) = \int_{y \in S} dy \, \exp\left[\frac{i\pi(x-y)^2}{\lambda D_1}\right] \exp\left[\frac{i\pi(y-z)^2}{\lambda D_2}\right], \quad (11)$$

modulo constant prefactors that drop out under $|U|^2$. The integrand is a Gaussian in y with complex coefficient, and after completing the square the integral can be evaluated analytically in terms of the Fresnel C and S functions.

The point-source / point-detector intensity $|U(x, z)|^2$ is not yet the observable signal. The thermal bulb illuminates a source slit of finite width and different points on the bulb-illuminated slit emit incoherently, so source-side averaging is incoherent. Similarly, the detector slit accepts light over a finite transverse width, integrating the intensity over that range. The final model prediction is therefore the triple integral

$$N(z_0) \propto \int_{-a/2}^{+a/2} dx \int_{z_0-a/2}^{z_0+a/2} dz \, |U(x, z)|^2, \quad (12)$$

where z_0 is the detector-slit centerline. The inner integral over y is coherent (this is what gives rise to interference), while the outer integrals over x and z are incoherent (these smear the fringes).

B. Fraunhofer Comparison

The Fraunhofer model can be recovered from Eq. (11) by dropping the y^2 terms in the expanded square roots, keeping only the linear-in-y contributions that produce the familiar $\sin\theta$ angular dependence. This further approximation is valid when the slit aperture is small compared to the Fresnel zone size $\sqrt{\lambda D}$. For our geometry $\sqrt{\lambda D_2} \approx \sqrt{(546 \text{ nm})(500 \text{ mm})} \approx 0.52$ mm, which is much larger than the single-slit width $a \approx 0.085$ mm but *comparable to* the double-slit separation $d \approx 0.40$ mm. The Fraunhofer approximation should therefore work well for the single-slit envelope but break down in the double-slit case, where the relevant transverse scale is the slit separation rather than the slit width.

This is exactly what we observe. For both single-slit scans the Fraunhofer and path-integral fits are statistically indistinguishable, differing in the fitted slit width a by less than the uncertainty on either value. In the double-slit scan, however, the Fraunhofer fit yields $\chi^2/\nu = 31.2$ with visibly systematic residuals at every fringe peak — the model consistently over-predicts the maximum intensities — while the path-integral fit yields $\chi^2/\nu = 4.3$, a more than sevenfold improvement, with no obvious residual structure aligned with the fringe locations. The path-integral fit also returns a slit width $a = 83.1 \pm 0.2$ μm that is consistent with the nominal value of 85 μm and with the values fit from the two single-slit scans ($a = 84.2$ and 82.3 μm), whereas the Fraunhofer double-slit fit absorbs the model mis-specification into an unphysically reduced slit width of $a = 79.4 \pm 0.2$ μm. The fitted slit separation $d \approx 400$ μm is consistent with the 0.406 mm assembly.

The remaining $\chi^2/\nu = 4.3$ in the path-integral double-slit fit is small enough to suggest model adequacy but large enough to indicate that one or more sub-dominant effects is still uncorrected. The strongest candidate is the finite spectral bandwidth of the green filter (541–551 nm), which we have neglected in favor of a monochromatic approximation at $\lambda = 546$ nm. A 10 nm bandwidth corresponds to a 2% spread in fringe spacing across the pattern, enough to wash out the deepest minima — which is precisely where the largest residuals are observed.

C. Coherent-Source Cross-Check with the Laser

To validate the apparatus alignment and modeling pipeline independently of the single-photon regime, we also recorded scans in laser-illumination mode using the photodiode detector. The laser source ($\lambda = 670$ nm) produces a coherent, high-intensity beam, giving photodiode voltages in the hundreds-of-mV range rather than counts per second. We recorded three scans paralleling the single-photon dataset: two single-slit envelopes with the slit-blocker covering the near and far slits in turn, and one double-slit fringe pattern. The same Fraunhofer and path-integral models were fit, with only the wavelength

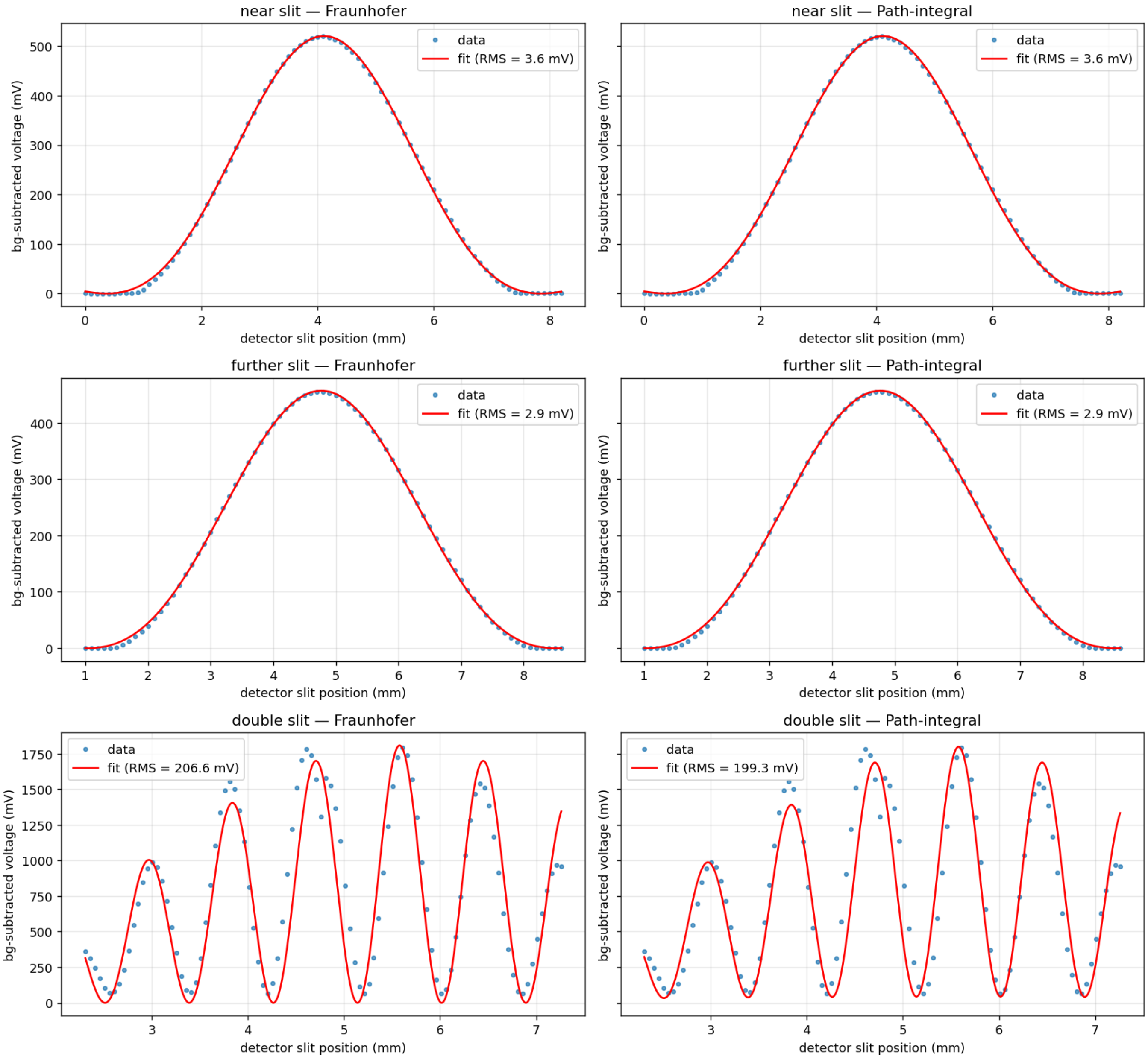

FIG. 5. Laser-illumination diffraction scans, used as a coherent-source cross-check. Top row: single-slit envelope recorded with one slit blocked; bottom row: double-slit fringes. Left column shows Fraunhofer fits, right column shows path-integral fits. Data are background-subtracted photodiode voltages. RMS residuals are reported in each legend; statistical parameter uncertainties are not shown because the stated meter reading precision does not reflect the dominant systematic scatter in the data. Fitted slit widths agree between models and between detection modes; the path-integral / Fraunhofer distinction is small in laser mode as expected from the lower Fresnel parameter relative to the bulb-mode analysis.

and data normalization changed; we used unit weights and report the RMS residual as a measure of fit quality, since the stated multimeter reading precision does not reflect the dominant point-to-point scatter in the data.

The results, shown in Fig. 5, qualitatively reproduce the single-photon-mode findings. Both single-slit fits return slit widths near the nominal 85 μm, with sub-percent RMS residuals on peaks of several hundred mV. The Fraunhofer and path-integral models are statistically indistinguishable on the single-slit data, as expected from the small Fresnel parameter $a/\sqrt{\lambda D_2} \approx 0.16$ for single-slit geometry.

The double-slit fits favor the path-integral model marginally but with a much smaller relative improvement than was seen with the bulb data. This is also expected: at $\lambda = 670$ nm the Fresnel parameter $d/\sqrt{\lambda D_2} \approx 0.66$ is closer to the Fraunhofer limit than the corresponding value for the bulb (≈ 0.77), and the two models therefore make more similar predictions in laser mode. The fitted slit separation $d = 383\ \mu$m differs from the bulb-mode value of $\approx 400\ \mu$m by about 4%, which is much larger than any per-fit statistical uncertainty and most likely reflects apparatus-level systematics that vary between measurement sessions: micrometer zero offset, double-slit re-positioning, or accumulated mechanical drift. The double-slit laser fit also shows a visible systematic in the residuals — the model's fringe spacing is slightly off from the data's, accumulating phase across the pattern — which most likely points to a small miscalibration in either the assumed laser wavelength or the double-slit-to-detector distance D_2. These cross-checks confirm that the apparatus and modeling are internally consistent at the several-percent level, and that the path-integral / Fraunhofer distinction we identified in the single-photon analysis is most pronounced precisely where the Fresnel parameter predicts it should be.

VI. CONCLUSION

We have performed an experiment to record interference patterns from single, filtered-bulb photons traversing one or both slits of a 0.085 mm double-slit assembly. By comparing the central-maximum count rate to the photon time-of-flight through the apparatus, we established that the probability of two photons occupying the apparatus simultaneously is of order 10^{-9}, placing the experiment firmly in the single-photon regime. Direct verification of Poisson photon-arrival statistics from $n = 8$ repeated 1-second counts at 28 detector positions confirmed that standard χ^2 fitting with Poisson weights $\sigma_i = \sqrt{n_i}$ is well-justified for our data.

The recorded patterns were fit to two models: the textbook Fraunhofer far-field expression $I(\theta) = I_0 \cos^2 \beta\, (\sin \alpha/\alpha)^2$, and a path-integral (Fresnel) model derived from Feynman's sum-over-paths prescription, accounting for the finite distances between source slit, double slit, and detector and for the finite widths of the source and detector apertures. Both models reproduce the single-slit envelopes to within statistical uncertainty, returning slit widths $a = 82$–$84\ \mu$m consistent with the nominal 85 μm. On the double-slit data, however, the path-integral model outperforms Fraunhofer by nearly a factor of seven in χ^2/ν (4.3 vs. 31.2) and recovers a slit width ($a = 83.2 \pm 0.2\ \mu$m) consistent with the single-slit fits, while Fraunhofer absorbs its model misspecification into an unphysically reduced a. This behavior is quantitatively predicted by the Fresnel parameter $F = L_\perp/\sqrt{\lambda D}$: for the double-slit case $F \approx 0.77$, large enough that the quadratic y^2 phase term discarded by the Fraunhofer approximation is non-negligible. Cross-checks against laser-illuminated data confirm the same picture, with the model distinction muted at the laser's longer wavelength as expected.

Despite the demonstrably wave-like character of the data — bright and dark fringes whose spacing follows the wavelength-dependent predictions of diffraction theory — every photon arrived at the detector as an individual, discrete event. The apparatus thus puts in direct confrontation the two complementary aspects of light's nature, and lends concrete experimental support to the quantum-mechanical picture in which interference is not a property of two waves superposing in space, but of probability amplitudes for indistinguishable paths combining coherently at the detector.

[1] T. Young, *A Course of Lectures on Natural Philosophy and the Mechanical Arts* (Joseph Johnson, London, 1807).

[2] A. Einstein, Über einen die erzeugung und verwandlung des lichtes betreffenden heuristischen gesichtspunkt, Annalen der Physik **322**, 132 (1905).

[3] G. I. Taylor, Interference fringes with feeble light, Proceedings of the Cambridge Philosophical Society **15**, 114 (1909).

[4] W. Rueckner and J. Peidle, Young's double-slit experiment with single photons and quantum eraser, American Journal of Physics **81**, 951 (2013).

[5] B. J. Luo, L. Francis, V. Rodríguez-Fajardo, E. J. Galvez, and F. Khoshnoud, Young's double-slit interference demonstration with single photons, American Journal of Physics **92**, 308 (2024).

[6] R. P. Feynman, R. B. Leighton, and M. Sands, *The Feynman Lectures on Physics*, Vol. III (Addison-Wesley, Reading, MA, 1965).

[7] S. J. Ling, J. Sanny, and W. Moebs, University physics volume 3, chapter 4: Diffraction, OpenStax (2016), `https://openstax.org/books/university-physics-volume-3/pages/4-3-double-slit-diffraction`.

[8] Massachusetts Institute of Technology, Physics 8.02 course notes, chapter 14: Interference and diffraction, MIT OpenCourseWare (2007), `https://ocw.mit.edu/courses/8-02-physics-ii-electricity-and-magnetism-spring-2007/`.

[9] J. F. Kenney and E. S. Keeping, *Mathematics of Statistics, Part Two*, 2nd ed. (Van Nostrand, Princeton, NJ, 1951).